Shear banding in drained and undrained triaxial tests on a saturated sandstone: Porosity and permeability evolution

J. Sulem*, H. Ouffroukh

CERMES, Ecole Nationale des Ponts et Chaussées/LCPC, Institut Navier, 6 et 8 avenue Blaise Pascal, Cité Descartes, Champs-sur-Marne, 77455, Marne-La-Vallée, Cedex 2, France

Abstract

Detailed analysis of shear band formation and shear band microstructure formed in drained and undrained triaxial tests on Fontainebleau sandstone is presented. It is shown that under globally undrained conditions, local fluid exchanges inside the sample occur at shear banding resulting into a heterogeneous damage pattern along the shear band. At high confinement, pore pressure generation inside the band leads locally to fluidisation of the crushed material, which results into the formation of connected channels in the heart of the band. Image processing analysis is used for evaluation of porosity inside the shear band and estimation of the permeability is performed using the Walsh and Brace [The effect of pressure on porosity and the transport properties of rock. J Geophys Res 1984; 89 (B11): 9425–31] model. It is shown that, porosity increase as observed in the band at low confining pressure and porosity decrease as observed at high confining pressure are both accompanied by a reduction of permeability inside the shear band due to the increase of tortuosity and specific surface. However, this permeability reduction is much more important at high confining pressure and can reach values three orders of magnitude smaller than the permeability of the intact material.
© 2005 Elsevier Ltd. All rights reserved.

Keywords: Sandstone; Shear-band; Porosity; Permeability; Image analysis

1. Introduction

Transport properties of porous rocks such as permeability are strongly influenced by the deformation process and controlled by the evolution of the structure of the grain geometry and the pore space (volume, connectivity, tortuosity, shape, etc.). Shear bands which in brittle rocks are zones of localised intense damage appear as weaker than the surrounding rock. Depending on the initial porosity of the rock and on the stress level, compaction and strain hardening or, on the contrary, dilation and strain softening may occur. In the last decade, important experimental and theoretical studies have been made in this area for understanding deformation mechanisms and permeability evolution in granular rocks [1–15]. Shear localisation results from the coalescence near the peak stress of clusters of oriented microcracks due to Hertzian fractures initiated at grain contacts.

For rocks with a relatively large porosity ($>10\%$) under hydrostatic loading, it has been identified by many authors (e.g. [16,17]) that the volumetric strain curve exhibits an inflection point for a stress of several hundreds of MPa beyond which an important inelastic volumetric compaction occurs. Microstructural observations show that significant grain crushing and pore collapse is associated with the inelastic compaction. The high density of cracks in the shear band is comparable with that of samples 'homogeneously' deformed in the cataclastic flow regimes. Detailed observation of shear

---

*Corresponding author. Tel.: +33 1 64 15 35 45;
fax: +33 1 64 15 35 62.

E-mail address: sulem@cermes.enpc.fr (J. Sulem).

zones may thus give clues to understand the behaviour of rocks at large stress when pore collapse and grain crushing are important.

A challenging issue is the modelling of grain crushing phenomenon and its influence on the hydro-mechanical properties. Grain crushability can be included in the modelling procedure using discrete element analysis [18,19]. Discrete element models can mimic the macroscopic behaviour of real including elasticity, anisotropic damage, post-peak softening [20–22]. However, up to now these models do not consider the influence of the evolution of the microstructure in due course of the deformation process on the hydro-mechanical properties of the rock. More recently a continuous approach including a degradation law for the rock skeleton was proposed by Yuan and Harrison [23] in order to account for the effect of porosity evolution on the permeability.

In a previous paper [24] the porosity change of shear bands formed in dry samples of Fontainebleau sandstone of initial porosity of 21% tested in triaxial compression has been analysed using a simple evaluation technique. This technique was based on the concept of linear porosity applied to microphotographs of the shear zone. It was shown that for specimens tested under relatively low confining pressure (7 MPa), the porosity increases up to about 30% inside the band and decreases rapidly towards the initial value outside the band. This was interpreted as dilating shear banding at low confining pressure. For specimens tested under relatively high confining pressure (28 MPa), a different patterning was observed. A compacting zone with high grain crushing and low porosity (values between 2% and 19%) is observed in the centre of the band. This zone is surrounded by a dilating one with grain cracking and high porosity (upto 36%). However, as mentioned in this paper, this simple technique is time consuming and

tedious, and cannot be used for systematic analysis of a large database.

In the present study the same rock (Fontainebleau sandstone) is used and geometrical characteristics of the shear band (porosity, specific surface, grain size) are evaluated by using image-processing software. The previous study is also extended to fluid saturated samples tested in drained and undrained conditions. The influence of the fluid and of the drainage conditions on shear band formation and shear band microstructure is carefully examined. Several authors have used image analysis of the pore structure of sandstone for predicting the permeability (e.g. [25]). Usually these models are based on a reconstruction of a network of connected conductors, which requires the knowledge of the geometrical properties of the pores. The approach that we use here is more empirical. The permeability model of Walsh and Brace [26] is used to correlate porosity and permeability.

2. Experimental setting

A triaxial cell with internal diameter of 140 mm is used (Fig. 1). This cell can sustain a confining pressure up to 60 MPa. It contains a system of hydraulic self-compensated piston. The loading piston is then equilibrated during which the confining pressure builds up and directly applies the deviatoric stress. The axial and radial strains are measured directly on the sample inside the cell with two axial transducers and four radial ones of LVDT type (see section AA on Figs. 1 and 2). These internal devices allows in avoiding the main errors of strain measurements of devices external to the cell such as the compliance of the loading device, the tilting of the specimen and the bedding errors at the ends of the
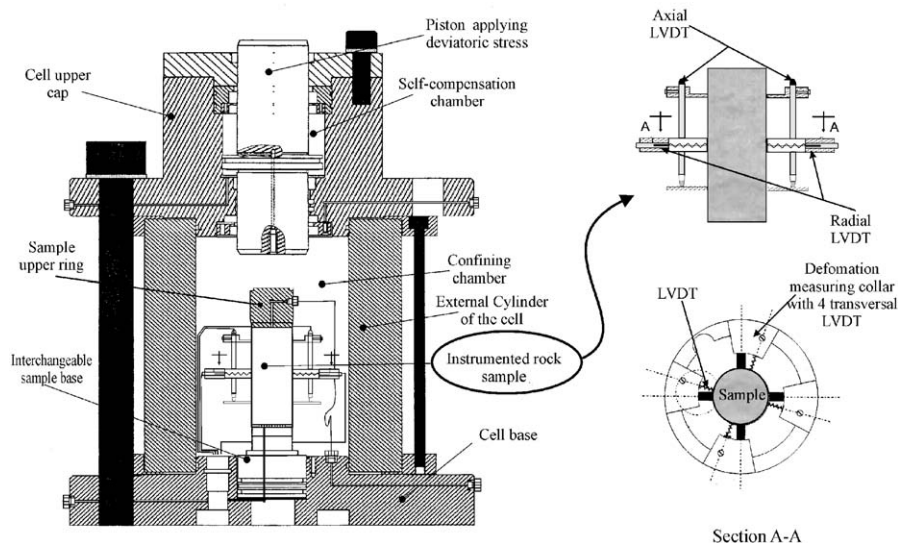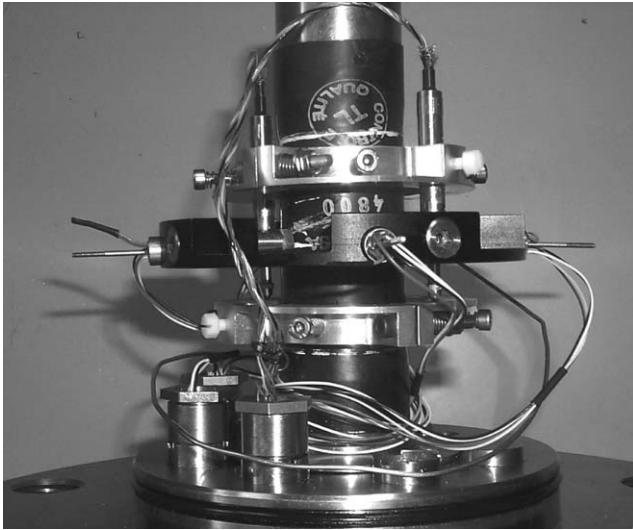

Fig. 1. Testing device.

Fig. 2. Instrumentation of the sample inside the cell.

Fig. 3. Microphotograph of an intact Fontainebleau sandstone.

specimen. This device is also more adequate that strain gages which are currently used for strain measurements on rocks. Strain gages can perturb the porous specimen because of glue penetration inside the sample and are useless beyond the onset of strain localisation. A correction for the radial deformation of the membrane during the test has been calibrated. The lower base of the cell is equipped with a pore pressure transducer. Pore pressure measurements during the test are then performed very close to the sample base. The confining pressure is applied by a servo-controlled high-pressure generator, which consists of a piston moving in a pressure chamber. The pressure generator is guided by an electronic regulator receiving an analogical signal from an external transducer. The regulators are programmed by a PC computer.

Axisymmetric strain-controlled compression tests in drained and undrained conditions have been performed on Fontainebleau sandstone at various confining pressures (7, 14, 28, 40 and 50 MPa). The axial displacement is servo-controlled via the internal radial transducers at a rate corresponding to a constant radial strain rate of $10^{-5}\,\text{s}^{-1}$ which is slow enough to insure fully drained deformation. The servo-control system allows to control failure and post-peak behaviour when the control parameters have been optimised for a fast response of the system [27]. The choice of the radial displacement as the control variable is made because this quantity is increasing rapidly with the axial stress close to the peak. The loading rate is thus actually very slow, close to the peak strength. The tests have been stopped soon after the maximum axial load has been reached in order to keep the samples in a state as close as possible to the shear band initiation and observe the bands after the tests with an electron scanning microscope as
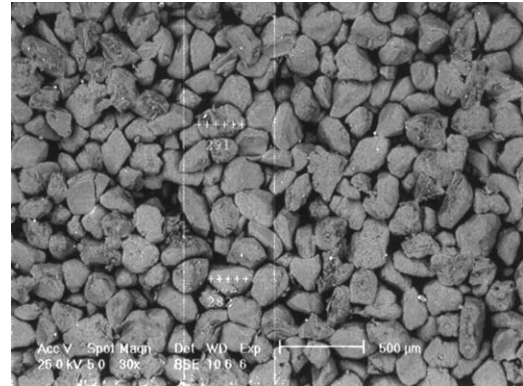
described in Section 4. In order to make a good observation it is important to obtain at the end of the test a specimen with one or several bands clearly formed but without any material discontinuity. Failure along a unique shear band is actually obtained for confined tests at low confining pressure and eventually along several bands for tests at high confining pressure. The interface between the rock specimen and the loading platens of the testing machine is lubricated to avoid friction [28–30]. Cylindrical specimens with a diameter of 37.5 mm and a height of 77 mm are used.

The rock chosen for this study is the Fontainebleau sandstone with a porosity of 21%. It is a uniformly graded rock with a grain size of 0.25 mm (Fig. 3). Its composition is 98% quartz.

3. Experimental results

3.1. Stress–strain response

In the range of confining pressures used in our tests the behaviour of Fontainebleau sandstone is rather brittle. The tests have been stopped just after the peak of axial load. The corresponding axial strain is around 0.5% for low confining pressure and 1% for higher ones. The overall stress–strain response is presented on Fig. 4 for drained tests and on Fig. 5 for undrained tests. We observe that for the undrained test at 7 MPa of confining pressure, the axial strain is decreasing after the peak whereas the radial strain is always increasing (Fig. 5a). As explained above, the radial displacement is actually the control variable of the system and it is increased at constant rate. The decrease of the axial displacement after the peak stress as measured by the transducers reflects the strain localisation process. When shear banding occurs the strain field is not homogeneous inside the sample and rigid block sliding along the shear surface can occur.
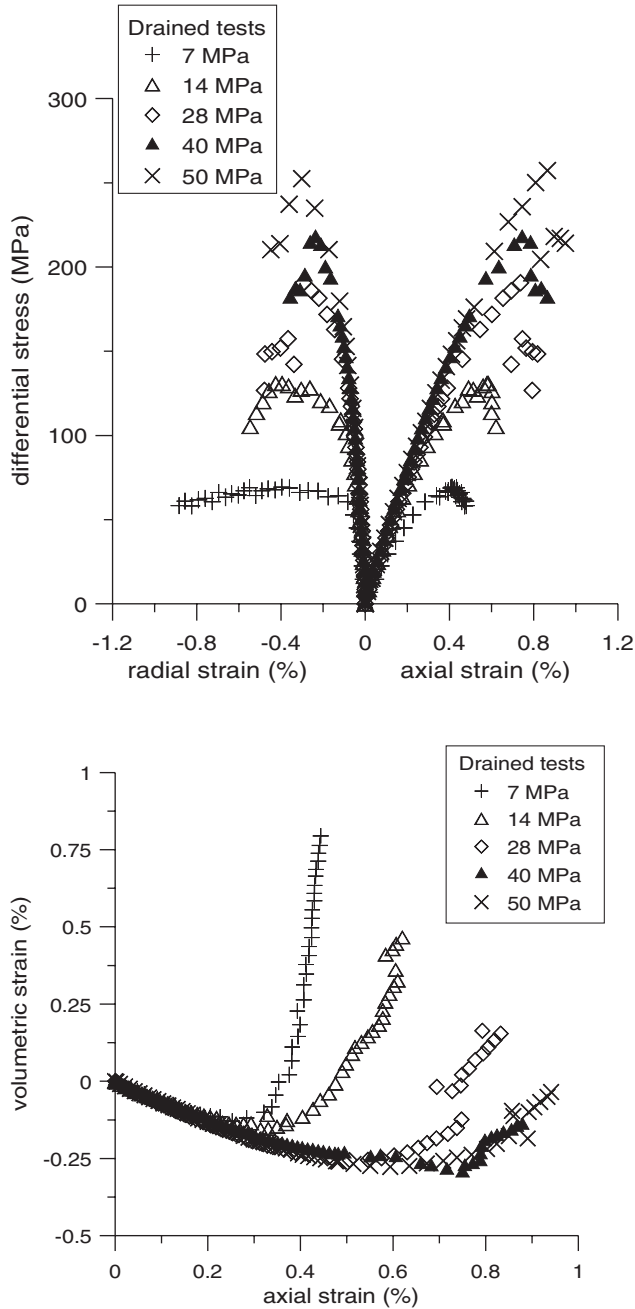
Fig. 4. Drained tests: deviatoric stress and volumetric strain versus axial stress.

respond to contractant (respectively, dilatant) behaviour. The samples undergo initial compaction and then dilatant strain hardening. The contractant phase is less pronounced for undrained tests due to pore pressure generation.

The experimental results for drained and undrained tests on saturated samples are consistent with those presented in Ref. [24] for dry samples (Fig. 6). The effective yield stress can be fitted with a linear Mohr–Coulomb criterion which in case of axisymmetric compression is written as

$$\sigma'_{axial} = 2C \tan(\pi/4 + \phi/2) + \sigma'_{axial} \tan^2(\pi/4 + \phi/2) \quad (1)$$

with

$$C = 15.5 \, \text{MPa} \quad \text{and} \quad \phi = 41.3°. \quad (2)$$

3.2. Pore pressure generation in undrained tests

The generated pore-pressure in undrained tests is plotted versus the axial strain for the various confining pressures on Fig. 5c. The magnitude of the induced pore pressure in the contractant phase depends upon the porosity of the rock, the drained compressibility of rock, and the compressibilities of the pore fluid and rock grains as described in Ref. [31]. Theses curves are consistent with the volumetric response of the samples (Fig. 5b). They exhibit a maximum at the contractance–dilatance transition. Dilatancy is caused by the formation and extension of open microcracks which results in pore pressure dissipation. The maximum of the generated pore pressure increases with increasing confining pressure. At low confining pressures (7 and 14 MPa) the pore pressure at yield effective stress is lower than the initially applied backpressure. Such cavitation phenomenon has been observed for dense sand [32] and for sandstone under low confining pressure [33].

3.3. Shear band formation

For all the tests in drained and undrained conditions, the specimens failed with the formation of one or several shear bands. In most experiments it was possible to control the post-peak behaviour and the unloading phase of the sample in order to avoid the formation of a discontinuity surface. These shear bands are clearly visible on the surface of the sample. The zone of localised failure is clearly identified due to the white colouration of the band visible to the naked eye (Fig. 7). Similar colourations of the shear zone in sandstone was observed by Ord et al. [13], Bésuelle et al. [12], Mair et al. [9] and El Bied et al. [24]. This colour change is due to the crushing of quartz grains and allows for a precise

Use is made here of the Terzaghi effective stress concept. Note that due to the fact that the fluid compressibility ($4.0 \times 10^{-4} \, \text{MPa}^{-1}$ at 20 °C) and the quartz grain compressibility ($2.75 \times 10^{-5} \, \text{MPa}^{-1}$) are comparable to the saturated rock compressibility ($10^{-4} \, \text{MPa}^{-1}$), undrained tests are not isochoric (i.e. at constant volume) as in classical Soils Mechanics (Fig. 5b). The maximum effective stress is increasing with effective confining pressure. On these graphs, negative (respectively, positive) volumetric strains cor-
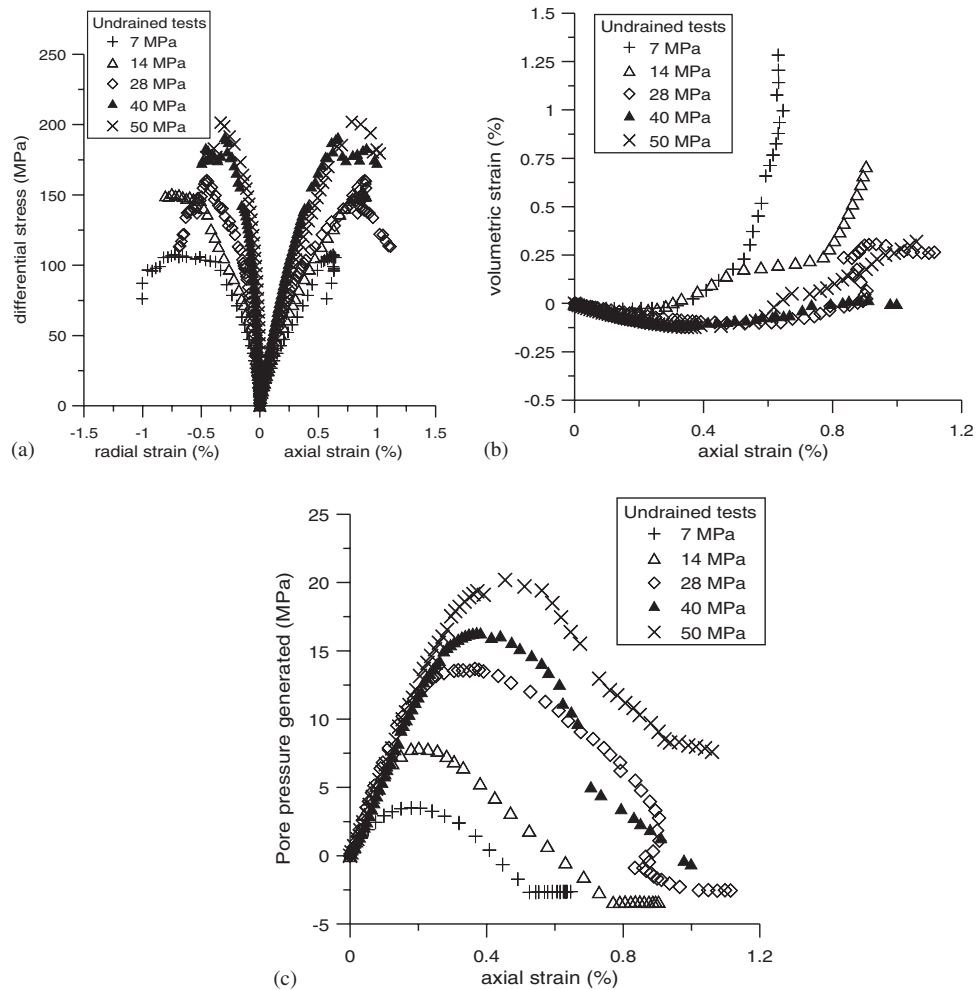
Fig. 5. Undrained tests: deviatoric stress, volumetric strain and pore pressure versus axial stress.
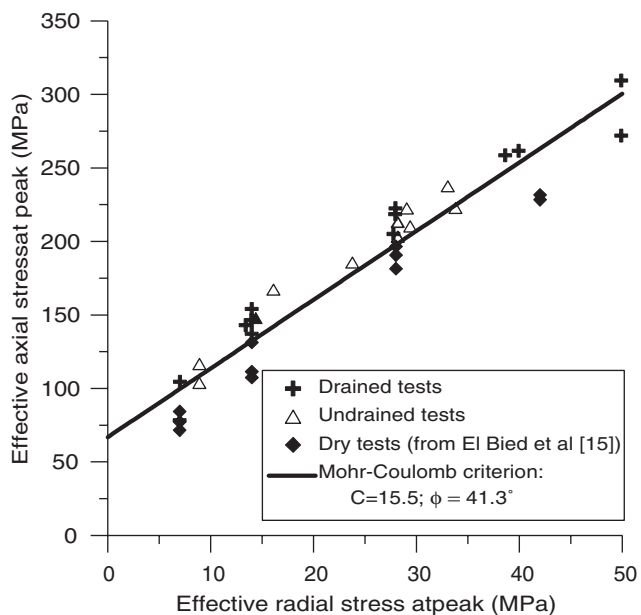

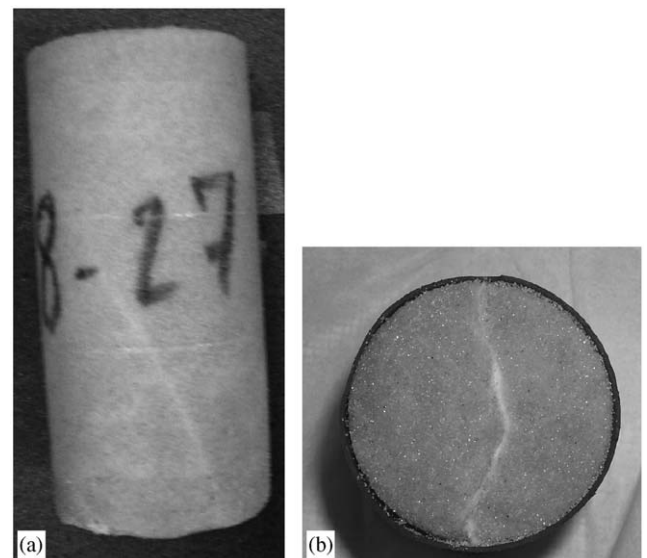Fig. 6. Failure criterion for drained and undrained tests.

Fig. 7. Lateral and radial surface of samples with a shear-band: (a) undrained test under 7 MPa of confinement, (b) drained test under 28 MPa of confinement.

evaluation of the thickness and the orientation of the shear band.

Extensive presentation of shear band analysis in geomaterials can be found in Vardoulakis and Sulem [34]. In globally undrained conditions, the heterogeneity of the damage pattern at shear banding as it will be presented in the next section, allows for local fluid exchanges. This means in turn that the heterogeneous development of microfractures in a granular rock during deviatoric loading leads to local drainage of the pore fluid. As shown by Vardoulakis [35,36] (see also Vardoulakis and Sulem [34]), the possibility of locally undrained shear banding is excluded as this situation would induce pore-water pressure shocks across the shear band boundaries.

The onset of shear banding has been studied experimentally using the independent axial and lateral displacement measurements on the specimen. Detection is performed by comparing the two axial strain measurements and/or the four radial strain measurements. The difference between the measurements of two opposite points is plotted versus the applied axial strain as shown for example in Fig. 8. This difference is very small and almost constant as long as the deformation is reasonably homogeneous inside the sample but diverges rapidly at some critical point corresponding to the threshold of loss of homogeneous deformation. This point indicates the limit after which the response of the specimen cannot be considered as representative of the material behaviour but as a structural response of a system. Without precise monitoring of the displacement field inside the sample during the test using visualisation techniques it is not possible to know if this point is the onset of the coalescence of localised damage zones or the onset of movement along a through-going shear band.

In Fig. 8 corresponding to a drained test at 28 MPa of confinement, the points of divergence for axial and radial strain measurements (points C_1 and C_2, respectively) are almost simultaneous and are compared with the threshold of contractant/dilatant behaviour (point B) and the point of loss of linearity of the axial strain–axial stress response (point A). A similar technique for the detection of strain localisation has been used by Santarelli [37], Tatsuoka and Kim [38] and Bésuelle et al. [12]. The results for all the tests are shown in Fig. 9. The axial and the radial measurements give in general similar results. The loss of homogeneous deformation occurs before the peak and is delayed at higher confining pressure in globally undrained conditions. In Fig. 10, the threshold from contractant to dilatant behaviour is compared with the onset of localisation for drained and undrained tests. This graphs shows that for drained tests the transition from contractant to dilatant behaviour, which corresponds to the initiation of microcracking occurs close before the onset of localisation. For undrained tests, due to the
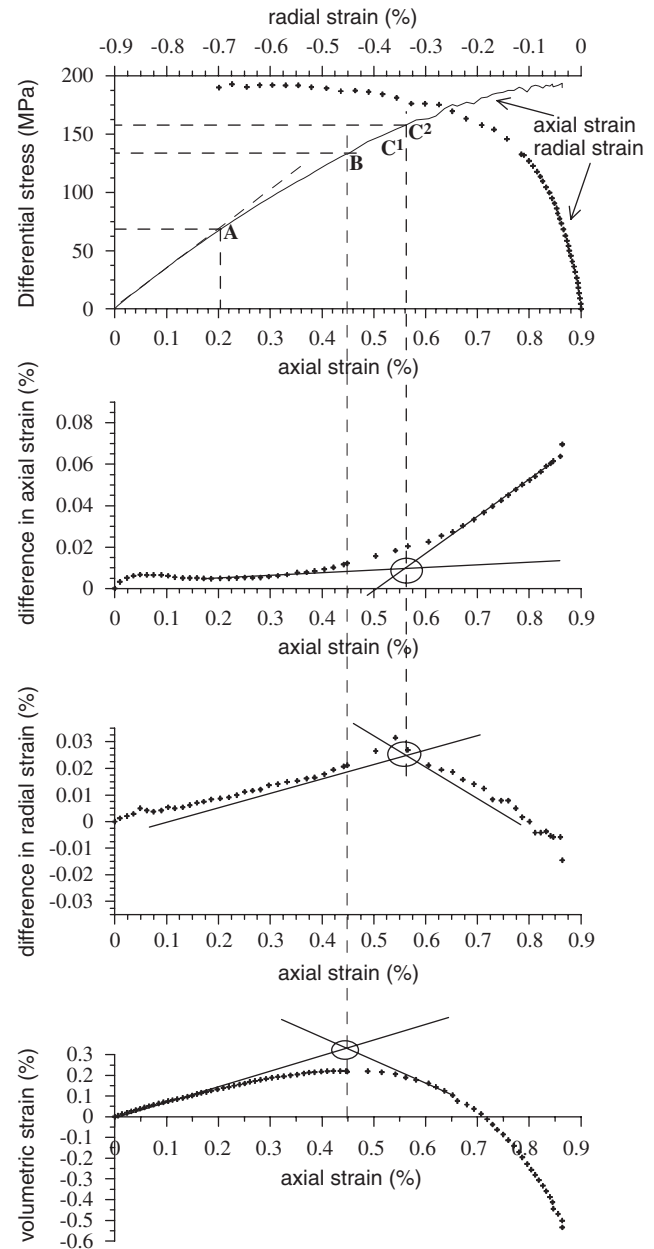

Fig. 8. Example of determination of the threshold of loss of homogeneous deformation (drained test at 28 MPa of confining pressure).

effect of pore pressure generation, the transition from contractant to dilatant behaviour occurs much earlier than for drained tests and is increasing for higher confining pressure. These two thresholds are observed not only for sandstones but also for crystalline rocks with the crack initiation and crack damage thresholds as defined for example for granite [39,40].

The orientation of the shear band is measured on the central part of the specimen, as the shear band is often deviated close to the extremities of it. The measured orientation of the shear band with respect to the minor
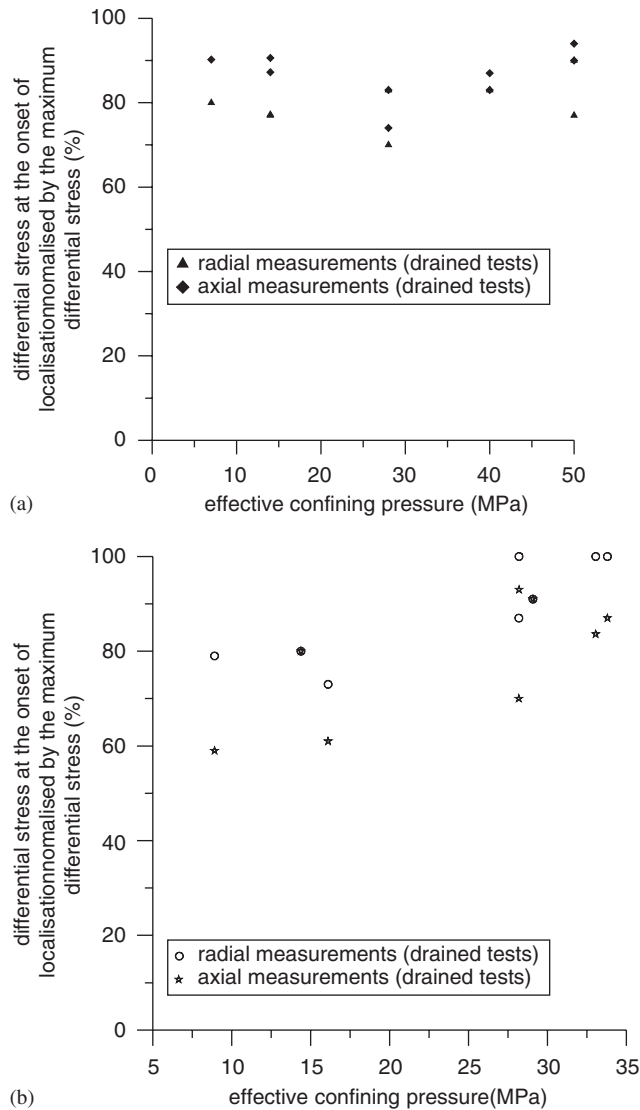
(a)

(b)

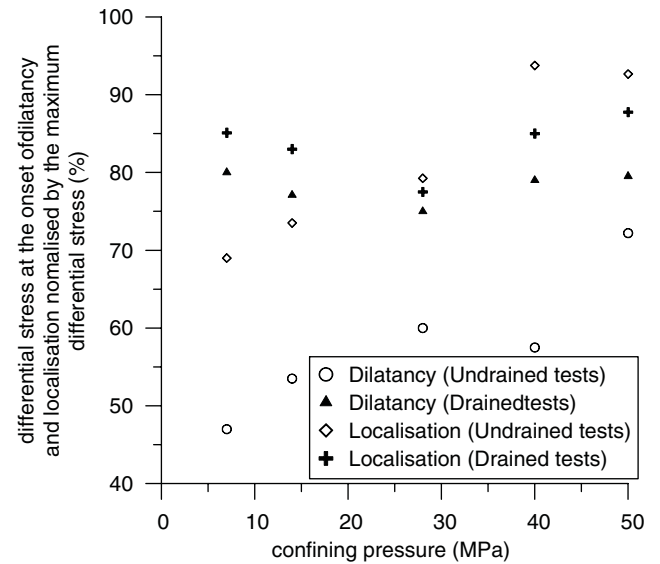Fig. 9. Onset of strain localisation: (a) drained tests and (b) undrained tests.

Fig. 10. Onset of dilatancy and onset of strain localisation.

Table 1
Shear band orientation for drained and undrained tests

Total confining pressure (MPa)	Shear band orientation drained tests (deg.)	Shear band orientation undrained tests (deg.)
7	69.7	70
14	63.4	69
28	61.9	66–68
40	57–60	63.5–66.5
50	54	60–62

(in absolute value) principal stress axis is presented in Table 1. These results show that the orientation of the shear band decreases when the effective confinement pressure increases as commonly observed (e.g. [12,24]). This can be explained by the pressure sensitivity of granular rocks for which the mobilised friction angle and dilatancy angle decrease with increasing effective mean stress. The difference observed in the shear band orientation between drained and undrained tests is due to the fact that in Table 1, the total confining pressure is referenced. As shown in the following, in terms of effective confining pressure, the results for undrained tests are consistent with those of drained ones (Fig. 12).

Strain localisation in the form of a shear band corresponds to weak discontinuities for the incremental displacement and occurs first when the acoustic tensor $\boldsymbol{\Gamma}$ becomes singular [41]:

$$\det(\Gamma_{ij}) = 0, \quad \text{with } \Gamma_{ij} = L_{ijkl}n_k n_l, \tag{3}$$

where $\mathbf{L}$ is the incremental constitutive tensor of the material and n_i are the cosines of the normal to the shear band.

As shown in Vardoulakis and Sulem [34], the shear band orientation $\theta_\mathbf{B}$ with respect to the major (in absolute value) principal stress axis can be approximated by a simple formula which was first proposed by Arthur et al. [42] on the basis of experimental observations and subsequently proven theoretically and supported experimentally by Vardoulakis [43] for biaxial tests:

$$\theta_\mathbf{B} = 45° + \phi/4 + \psi/4, \tag{4}$$

where ϕ is the friction angle and ψ is the dilatancy angle at the onset of strain localisation. In a simple analysis it is assumed that shear banding occurs at maximum deviatoric stress corresponding to a mobilised friction
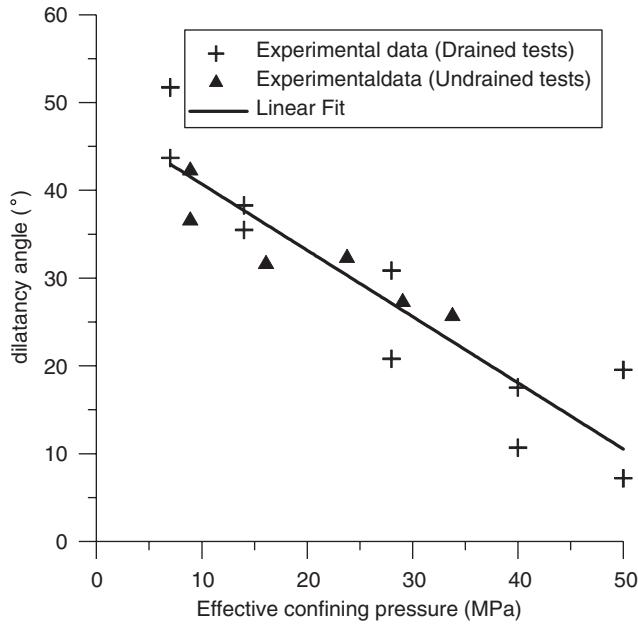
Fig. 11. Dilatancy angle versus effective confining pressure.

angle of 41.3°. The dilatancy angle is evaluated on experimental data at various effective stress. For drained and undrained tests, it is found that the dilatancy angle at peak stress evolves in a consistent manner with the effective confining pressure. Accordingly the data are fitted with the following linear relation (Fig. 11):

$$\psi(\text{in degrees}) = -0.76\sigma'_{rad}(\text{in MPa}) + 48.3, \qquad (5)$$

where σ'_{rad} is the effective radial stress expressed in MPa.

As shown in Fig. 12a the Arthur's formula gives an acceptable evolution of the shear band inclination with respect to the effective confining pressure.

Remark: For our tests in the range of confining pressures used, the maximum mobilised friction angle was found to be independent of the confining pressure and equal to 41.3. The classical Mohr–Coulomb solution for the orientation of the failure plane is $45° + \phi/2 = 65.65°$· The Coulomb solution cannot reflect the decrease of the shear band orientation with confining pressure. We show here the important effect of the dilatancy angle on the shear band orientation.

A more precise evaluation of the shear band orientation can be obtained by performing a complete strain localisation analysis which gives good predictions of the shear band inclination (Fig. 12b). The analysis is presented in Appendix A.
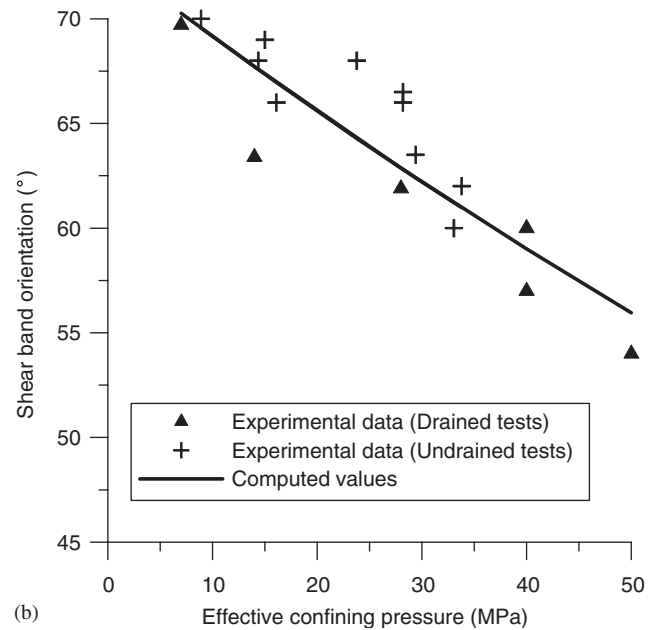
4. Microstructural observations

4.1. Sample preparation

As explained in Section 2, the test is stopped close after the peak strength. A good control of the post-peak
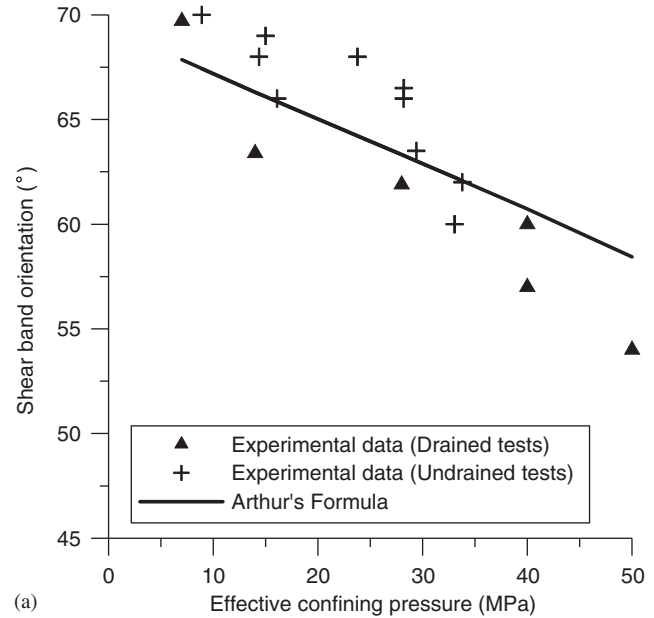
(a)

(b)

Fig. 12. Shear band orientation versus the minor principal stress for drained and undrained tests.

phase allows in avoiding a violent failure of the sample. Therefore the sample shows a clear shear band but no material discontinuity.

At the end of the compression test, each sample is carefully removed from the loading cell while still encased in its rubber sleeve and put into a vacuum bell jar where it is impregnated with epoxy resin. A plane cutting of the specimen allows a clear observation of the shear band inside the rock to evaluate its thickness and orientation. A metallisation is performed by pulverising gold. This operation allows better observations with the

electron scanning microscope. Examples of microphotographs of the shear band zone are presented for an undrained test under 7 MPa of confining pressure (Fig. 13) and a drained test under 50 MPa of confining pressure (Fig. 14).

4.2. Image analysis software

Image analysis is nowadays currently used to study rock microstructure (e.g. [2,3,25,44–46]). It is of major importance to have a good resolution of the input image and a good tuning of the contrast and of the threshold of grey level to discriminate between solids and voids and obtain reliable image analysis results. In this study the image analysis software 'IMAQ-VISION Builder 6' of National Instruments is used. Each image taken from the electron scanning microscope is represented by a grey level matrix with values between 0 and 255. A binary image is built by the choice of a threshold for the grey level which attributes the value 0 for voids and 1 for the solid phase. The proper choices of this threshold as well as the good resolution of the original image are key points to obtain good results in computer-aided image analysis. The ratio of magnification is chosen for each micrograph and the threshold of the grey level is first calibrated for each image by analysing the grey level histogram and by comparing the binary image and the original one (Fig. 15). In particular, one must insure that the small particles are not lost or clustered which are the main sources of inaccuracies for porosity evaluation. The binary image is then analysed for the determination of the porosity, the specific surface, the orientation and the size of the particles.
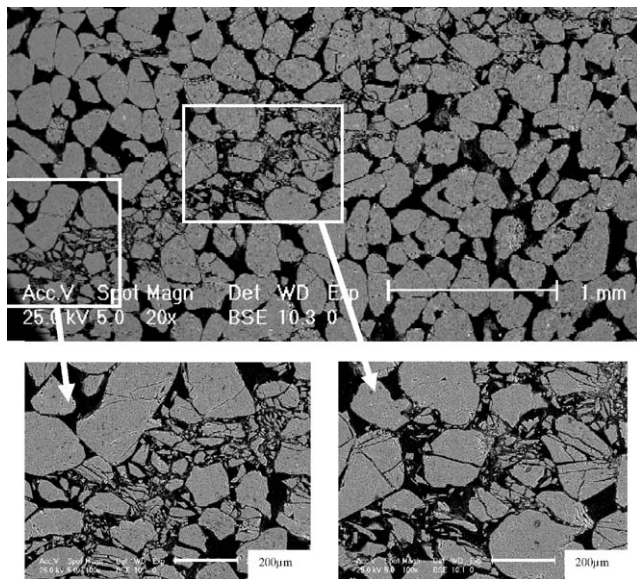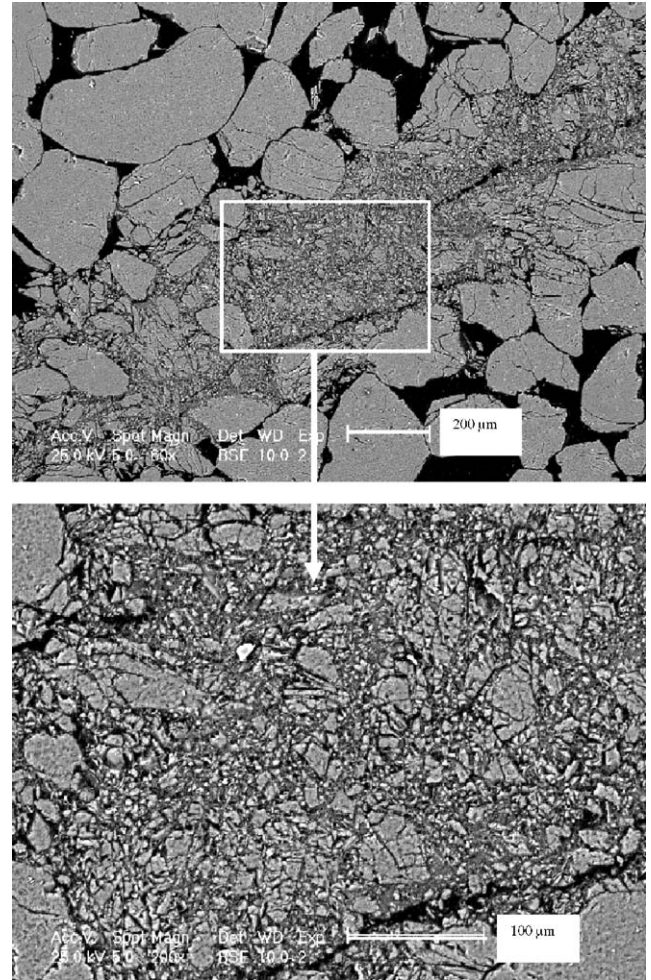

Fig. 14. Microphotographs of a shear band formed in a drained test under 50 MPa of confinement: general view and detail.

This technique was first applied to intact Fontainebleau sandstone specimens with different porosities between 7% and 20%. The results of the image analysis have been compared to the ones obtained from classical experimental porosity determination such as water imbibation and mercury intrusion (Table 2). They show a good agreement between the experimental technique and the image analysis determination. The specific surface is the pore surface area per unit volume. Image analysis of the intact Fontainebleau sandstone specimens is used to evaluate this quantity. The results have been compared to those published by Fredrich et al. [44] for Fontainebleau sandstone specimens with similar porosity and have also shown good agreement (Table 3).

4.3. Image analysis of shear zones

The structures of the shear zones for the specimens tested at relatively low confining pressure (7 and 14 MPa) are similar for drained and undrained tests

Fig. 13. Microphotographs of a shear band formed in undrained test under 7 MPa of confinement: general view and details.

(Figs. 13 and 16). The shear band thickness is comprised between 200 and 500 μm i.e. one to two intact grain size. Inside the band the grains are broken with little localised crushing.

For the specimens tested in drained conditions under higher confining pressure (28, 40 and 50 MPa) the shear band is characterised by intense grain crushing and pulverisation (Fig. 17). Major changes in the grain size distribution are clearly visible. Very small particles with size of the order of micrometers are produced. The fragments are densely packed, which gives an aspect of

Fig. 15. Example of binary image (b) obtained from the original grey level image (a).

flour or white powder visible to the naked eye. Similar observations have been made for dry specimens of Fontainebleau sandstone [24].

For specimens tested in undrained conditions under high confining pressure (28, 40, 50 MPa) the structure of the shear zone is quite heterogeneous with zones of compaction (as in the drained tests) and zones of dilation (Fig. 18). This heterogeneity can be related to the heterogeneity of the pore pressure generated during the loading of the sample. This results into local fluid exchanges between compacting zones that expel fluid and dilating ones that absorb it. The observations demonstrate also that, although no fluid exchanges is allowed between the sample and the exterior of the system during globally undrained tests, local fluid exchanges inside the sample occur at shear banding resulting into an heterogeneous damage pattern along the shear band. At high confinement, pore pressure generation inside the band leads locally to fluidisation of the crushed material which results into the formation of connected channels in the heart of the band (Fig. 19). In Fig. 19b one can clearly observe that the fines are accumulating along the boundary of the shear band and form a clogged zone of clustered fines. In our understanding the observed channels in undrained tests cannot be attributed to the formation of open fractures during unloading or resin impregnation process as such features are not observed in samples tested in drained conditions.

Outside the shear band, near the limits of the shear band, the grains are cracked but not crushed. The cracking phenomenon decreases rapidly outside the band.
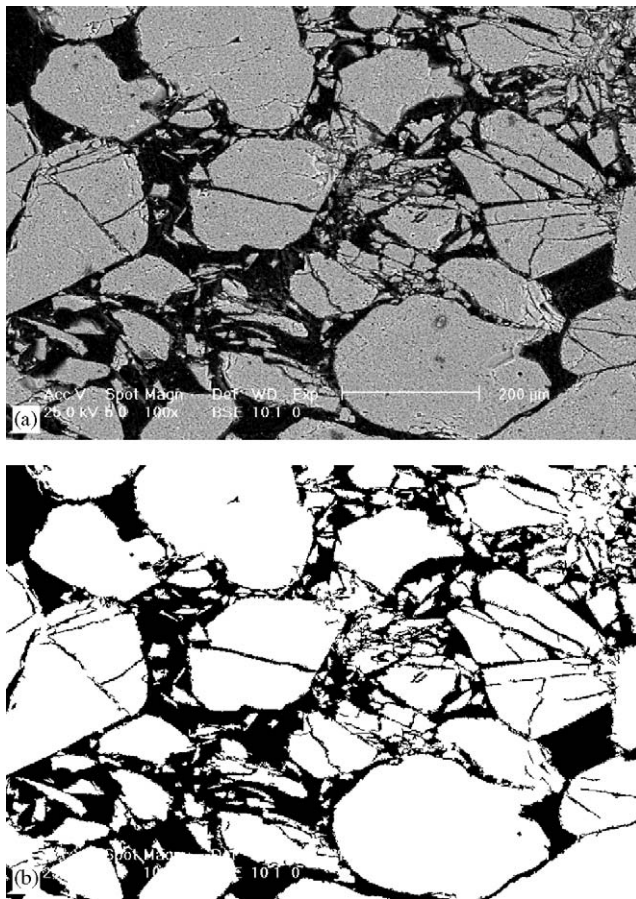
Table 3
Specific surface for Fontainebleau sandstone of various porosities (after Ref. [47])

Sample	Porosity (%)	Specific surface (mm^{-1})
F1	4.6	9.36 ± 2.76
F4	10.7	20.32 ± 4.76
F7	15.9	22.44 ± 3.64
F8	20.5	19.76 ± 2.28

Table 2
Measured and estimated porosity

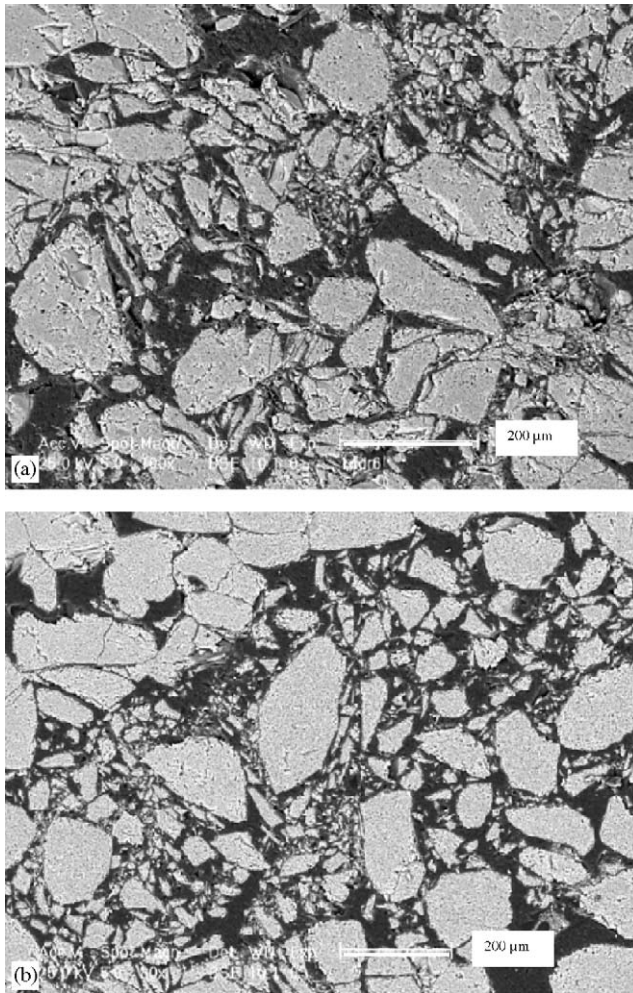| Test reference	Experimental measurements of porosity (%)		Image analysis	
	Water imbibation	Mercury porosimetry	Evaluated porosity (%)	Evaluated specific surface (mm^{-1})
877E	7.25	6.32	7.08	15.55
878B	11.24	10.62	9.6	15.06
878A	14.11	13.25	14.05	16.08
878E	17.12	19.74	17.63	19.29
878D	18.19	17.18	21.13	22.03

Fig. 16. Microphotographs of a shear band formed under 14 MPa of total confinement: (a) drained tests and (b) undrained test.

Fig. 17. Microphotographs of a shear band formed in drained tests: (a) 28 MPa, (b) 40 MPa and (c) 50 MPa.

From image analysis processing, the porosity of the material is evaluated at various places inside and outside the shear band. Inside the shear zones, the grain size distribution of the rock and the pore space are heterogeneous. Therefore the analysis is performed on ten different images taken at various locations along a parallel to the shear band axis. The porosity is evaluated for each image and the mean value is calculated. The size of each image on which the porosity is evaluated is about 20 intact grain sizes which can be considered as a representative element. An example of an image on which the porosity is calculated is shown in Fig. 20. This micrograph is a magnification of a zone of Fig. 17a. In a previous paper [24], the evolution of the grain size distribution inside the band was discussed. For example, it was shown that, for the specimen tested under 28 MPa, 74% of the particles have a size smaller than $D_{50}/10$ and 26% have a size comprised between $D_{50}/10$ and D_{50}. These numbers show that the dominant effect here is pulverisation of the grains. The smallest grain
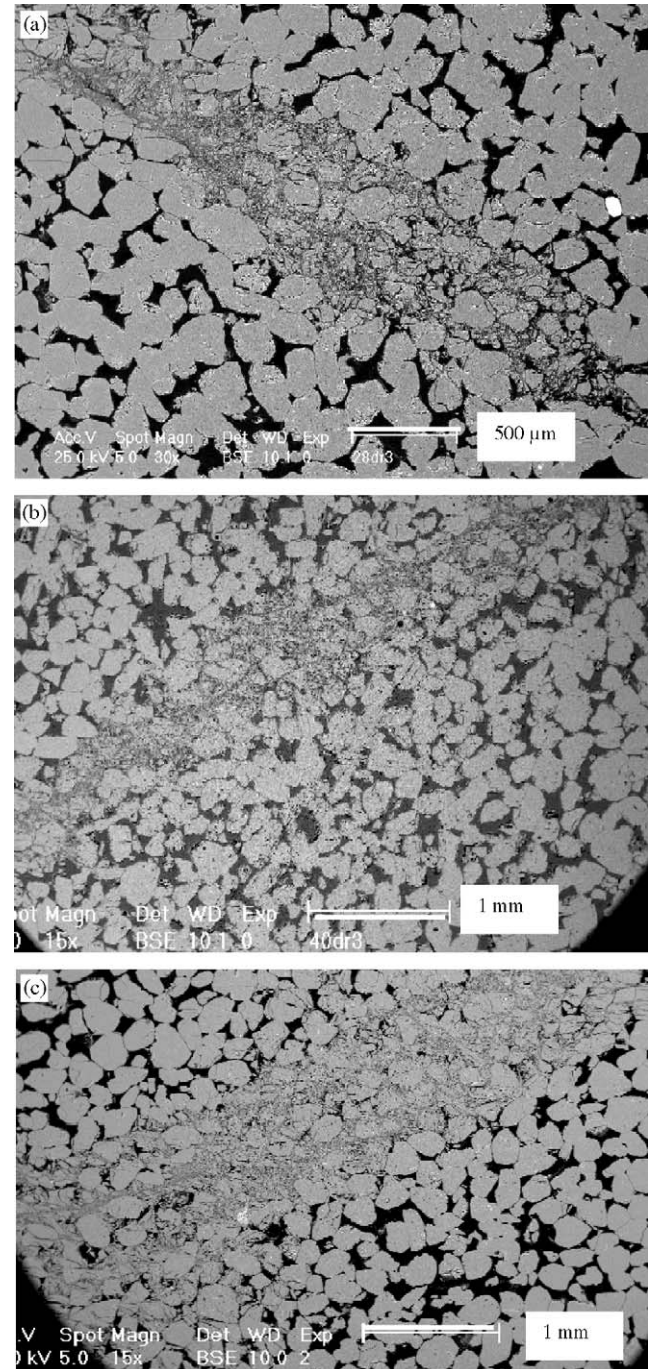
size observed is 1 μm. Only few grains are simply fractured. All grain size measurements are smaller that D_{50}. For the permeability evaluation proposed in Section 4, the permeability model of Walsh and Brace [26] used here does not include explicitly the grain size of the rock. The only geometric quantities involved are the porosity and the specific surface.
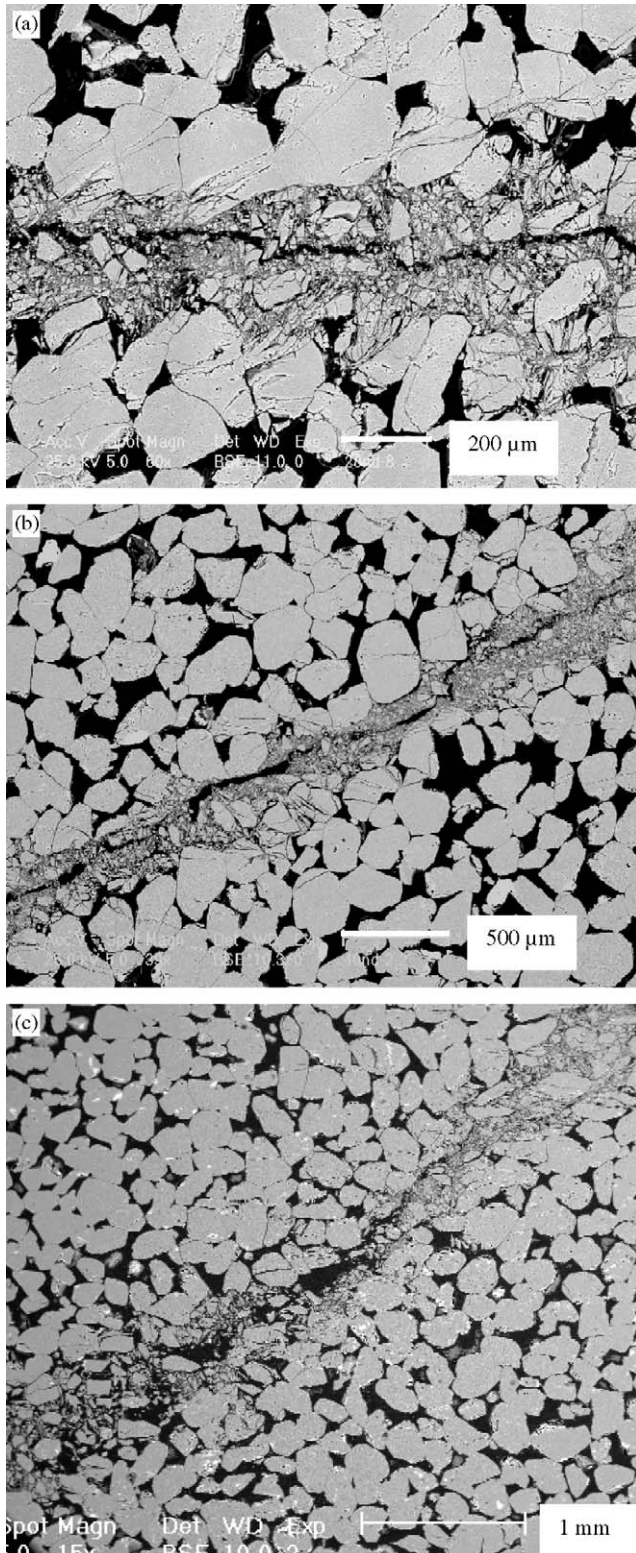
Fig. 18. Microphotographs of a shear band formed in undrained tests: (a) 28 MPa, (b) 40 MPa and (c) 50 MPa.

Fig. 19. Channels formed in undrained tests: (a) 28 MPa, (b) 40 MPa and (c) 50 MPa.

The results of the evaluation of the porosity inside the bands are shown in Fig. 21a for the drained tests and in Fig. 21b for the undrained tests. As in the undrained
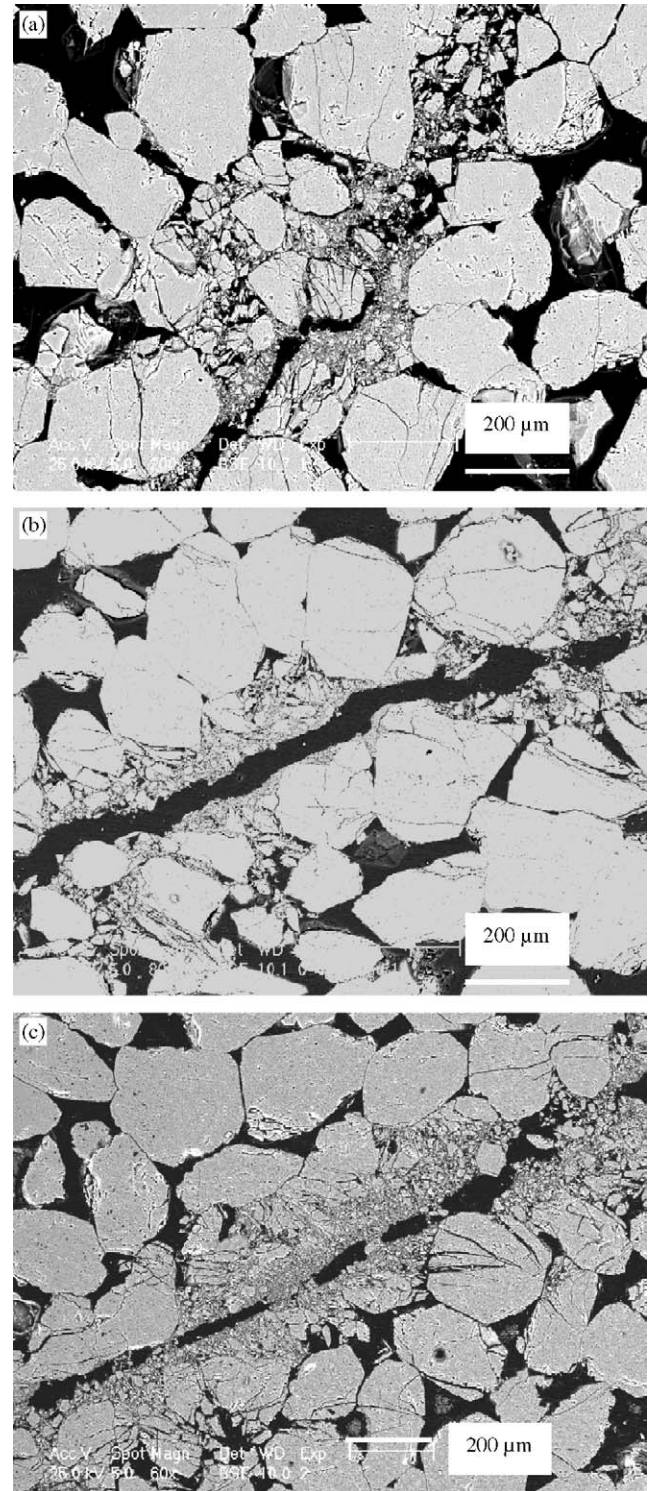
tests at high confining pressure it was observed that the structure of the band is heterogeneous with zones of dilation and zones of contraction; porosity evaluation on these specimens has been preferably performed on
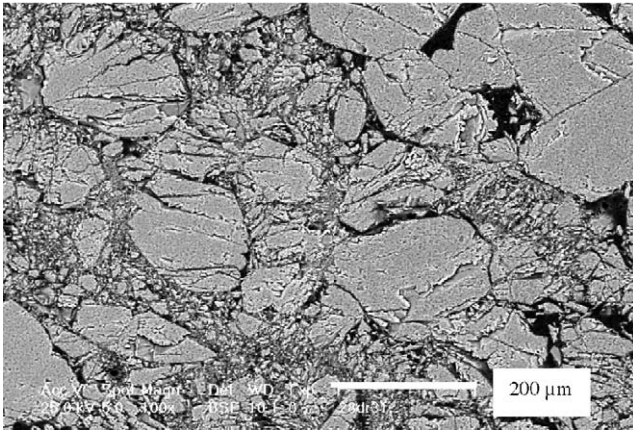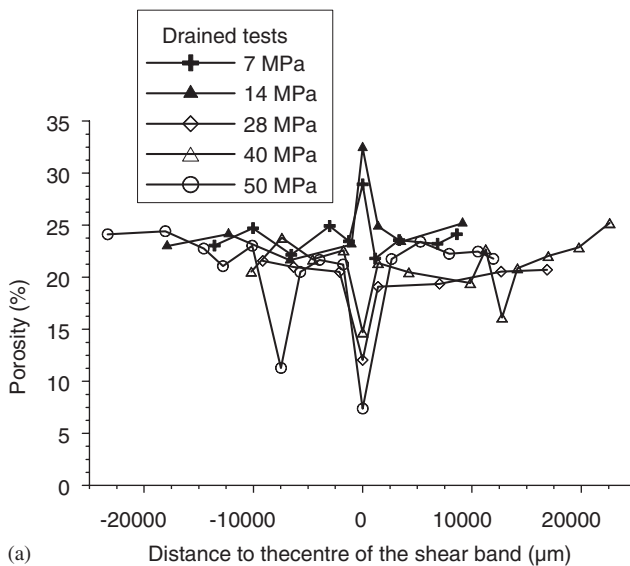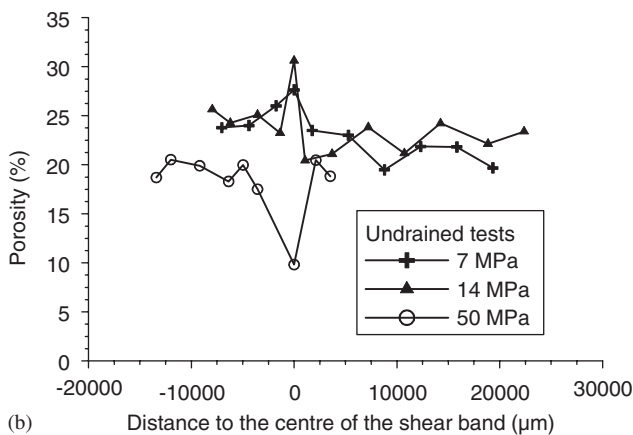
Fig. 20. Example of a image on which the porosity is evaluated.

Fig. 22. Average porosity evaluated inside the shear band for drained and undrained.

Fig. 21. Porosity evolution in the direction perpendicular to the major (in absolute value) principal stress axis: (a) drained tests and (b) undrained tests.

the compacting zones. The average porosity inside the band is plotted versus the confining pressure for drained and undrained tests in Fig. 22. For each confining
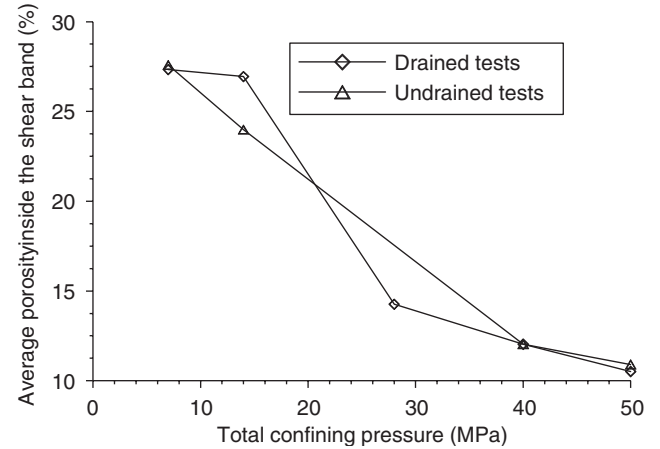
pressure the two values are very close. A sharp transition occurs for a critical confining pressure of about 20 MPa. At lower confining pressure for this critical value, the porosity inside the band is higher that the one of the original sample (here 21%). For higher ones it is smaller and reaches a value of about 10% for tests at 50 MPa of confinement (Table 4).

4.4. Permeability model

It is known that there is no unique relationship between porosity and permeability applicable to all porous media and that the geological evolution process of the pore space influences the permeability–porosity relationship (e.g. [11]). In classical permeability models such as the Carman–Kozeny model, the permeability is related to pore geometry parameters, i.e. porosity, hydraulic radius, tortuosity and specific surface. For the Fontainebleau sandstone, it was shown by Fredrich et al. [47] that the observed bench permeabilities for samples with porosities between 10% and 20% agree well with those using the equivalent channel model of Walsh and Brace [26] with the following expression for the permeability:

$$k = \left(\frac{n}{S_v}\right)^2 \frac{1}{Fb}, \tag{6}$$

where S_v is the specific surface, n the porosity, b is a shape factor and F is a formation factor given by

$$F = \frac{\tau^2}{n} = \frac{\rho}{\rho_f}. \tag{7}$$

In the above expression for the formation factor F, τ^2 is the tortuosity and ρ and ρ_f are the resistivities of the saturated rock and of the fluid, respectively. The shape factor b is equal to 2 for circular tubes and equal to 3 for cracks. The Archie [48] law is used to approximate the

Table 4
Measured and estimated permeability

Test reference	Evaluated porosity (%)	Evaluated specific surface (mm^{-1})	Estimated permeability (mDarcy) Walsh and Brace model ($b = 2$)	Estimated permeability (mDarcy) Walsh and Brace model ($b = 3$)	Measured permeability (mDarcy) (Eq. (10), after Ref. [49])
877E	7.08	15.55	128.5	85.6	118.6
878B	9.6	15.06	389.1	259.4	300.2
878A	14.05	16.08	1258.9	839.3	959.1
878E	17.63	19.29	1902.7	1268.5	1916.5
878D	21.13	22.03	2713.3	1808.9	3329.5

formation factor

$$F = \frac{\rho}{\rho_f} = \frac{a}{n^m}, \qquad (8)$$

where m is the cementation factor and a is a pore geometry coefficient.

Data published in the literature on measurements of pore geometry characteristics and transport properties of Fontainebleau sandstone samples of various porosities by Bourbié and Zinsner [49], David and Darot [50], Fredrich et al. [47] have been used to calibrate the various parameters of the Walsh and Brace [26] model.

The two parameters a and m are calibrated on data from Refs. [47,50]. The results are shown in Fig. 23. The following values have been found: $a = 1.844$, $m = 1.427$.

On the basis of a large database of 240 samples of Fontainebleau sandstone with various porosities, Bourbié and Zinsner [49] have proposed a power law relationship between the porosity and the air permeability:

$$k(m\text{Darcy}) = 0.303n^{3.05} \quad \text{for } n > 8 - 9\% \text{ and}$$

$$k(m\text{Darcy}) = 2.75 \times 10^{-5}n^{7.33} \quad \text{for } n < 8 - 9\%. \qquad (9)$$

The evaluation of permeability on image analysis of intact samples has been performed using the Eqs. (6–8) with $b = 2$ and $b = 3$ and compared to the power law relationship (9). The results are shown in Fig. 24. The evaluated permeability reproduce correctly the data of Bourbier and Zinsner [49]. These results validate the calibration procedure.

From the evaluation of porosity and specific surface inside the bands of our samples, the permeability has been estimated using the Walsh and Brace model with the above values of the parameters. The results are shown in Fig. 25 for drained tests and on Fig. 26 for undrained tests. In both cases the value of $b = 2$ is assumed. They are similar for drained and undrained tests. For high confining pressure with a compacted shear band, the porosity reduction is accompanied by an important permeability reduction of more than 3 orders of magnitude. For low confining pressure with a dilatant shear band, the porosity increase is accompanied also with a decrease of the permeability of 1–2 orders of magnitude. This counterintuitive result is due to the fact
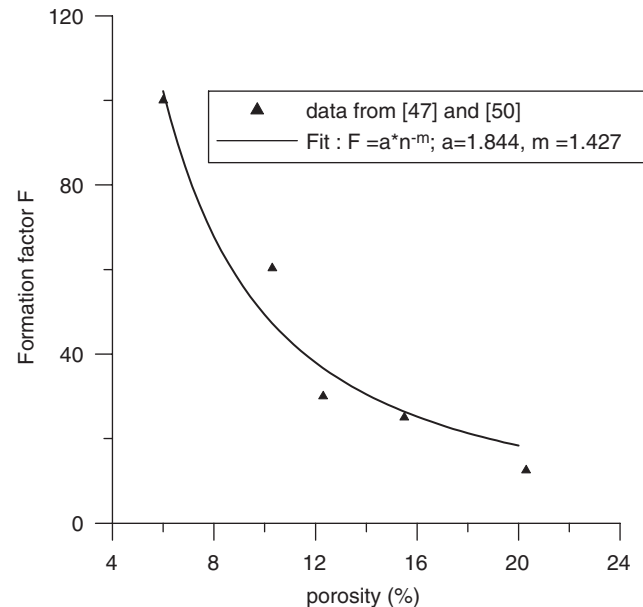

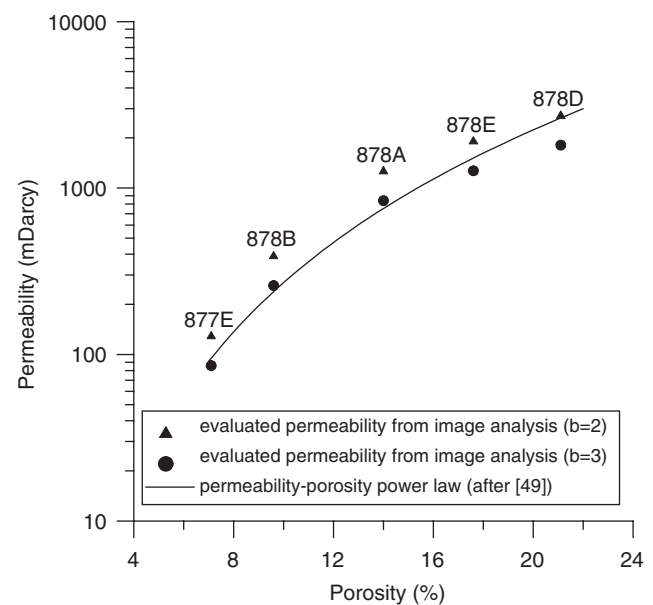Fig. 23. Evaluation of the formation factor.

Fig. 24. Permeability evaluation on intact samples and comparison with Bourbier and Zinsner [49] power law.
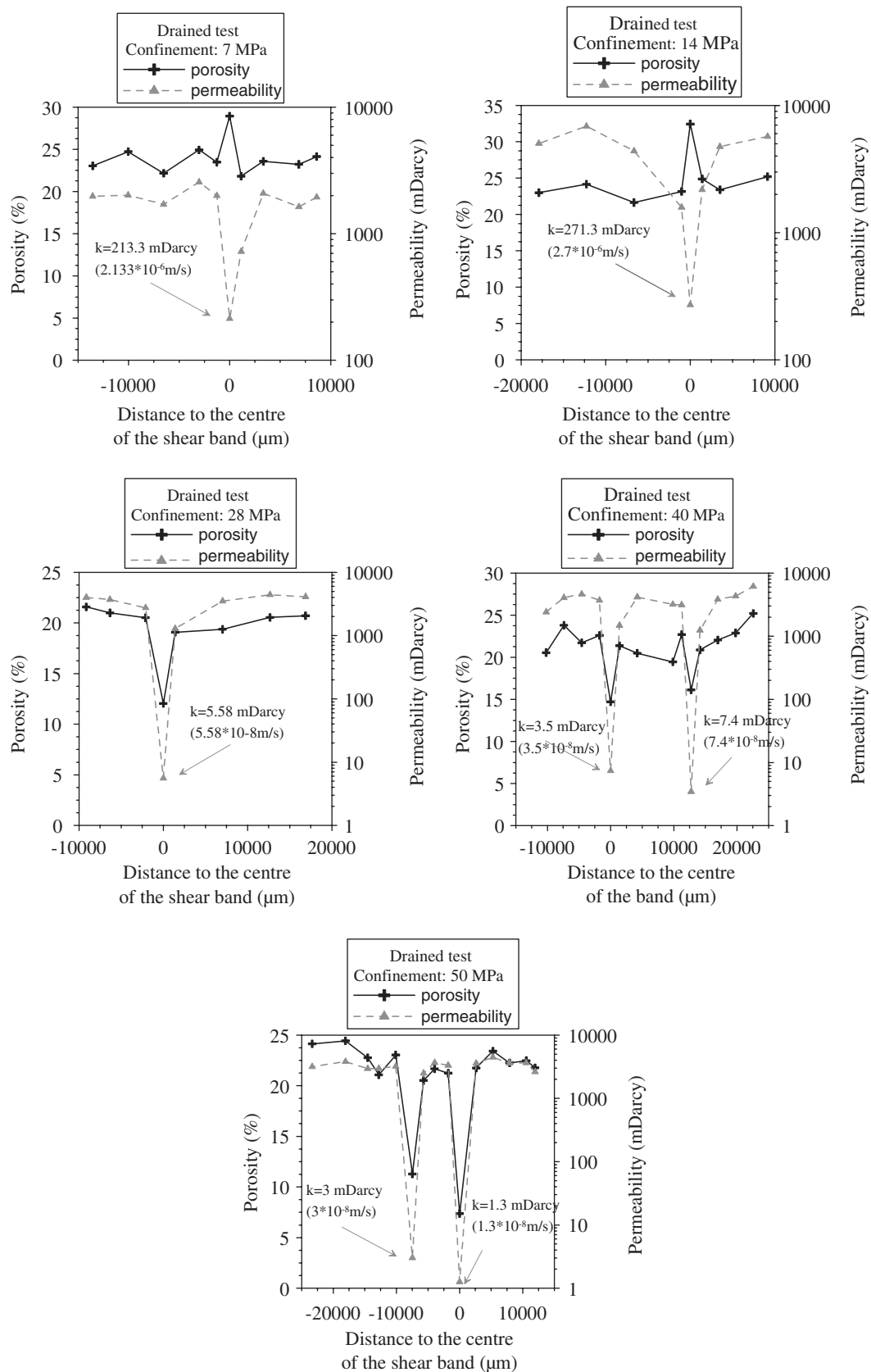
Fig. 25. Evaluation of the permeability inside the shear bands for drained tests.
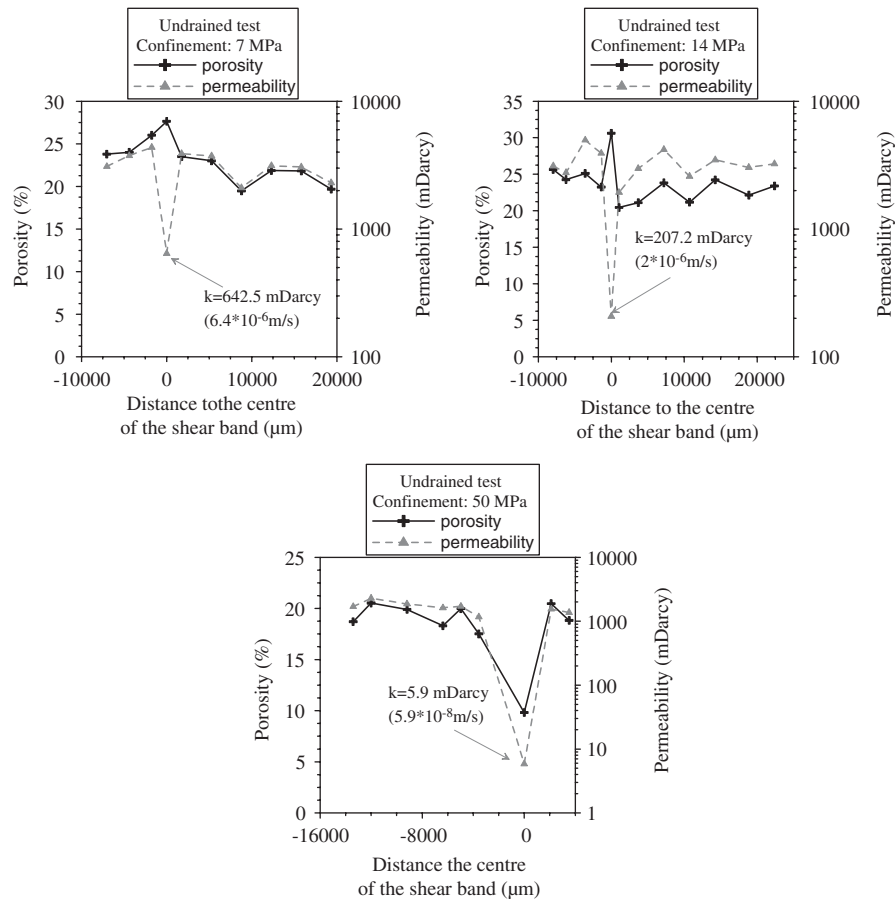
Fig. 26. Evaluation of the permeability inside the shear bands for undrained tests.

that despite the increase of porosity, the increase of the specific surface inside the band induces a permeability reduction. Similar observations have been made for sandstones with a porosity higher than 15% [5,6].

5. Conclusion

Transport properties of rocks such as permeability are strongly influenced by the deformation process. On the basis of image analysis, porosity, specific surface and grain size changes have been studied inside the shear bands formed in triaxial testing on a Fontainebleau sandstone with initial porosity of 21% under drained and undrained conditions at various confining pressures.

It is obtained that for specimens tested under relatively low confining pressure (7 and 14 MPa), the porosity reaches a maximal value of about 30% inside the band and decreases rapidly towards the initial value of 21% outside the band. This is interpreted as dilating shear banding at low confining pressure. For specimens tested under high confining pressure (>25 MPa), a different patterning is observed. A compacting zone

with high grain crushing and low porosity is observed in the centre of the band. The porosity reduction is more pronounced at higher confining pressures. From the porosity and specific surface data evaluated from image processing inside the shear zone, the changes in permeability are quantified by using the permeability model of Walsh and Brace [26]. It is shown that, porosity increase as observed in the band at low confining pressure and porosity decrease as observed at high confining pressure are both accompanied by a reduction of permeability inside the shear band due to the increase of tortuosity and specific surface. However, this permeability reduction is much more important at high confining pressure and can reach values 3 orders of magnitude smaller than the permeability of the intact material.

In globally undrained conditions, similar changes of microstructure of the rock are observed depending on the confining pressure. This results into local fluid exchanges between compacting zones that expel fluid and dilating ones that absorb it. The observations demonstrate also that, although no fluid exchanges is allowed between the sample and the exterior of the

system, local fluid exchanges inside the sample occur at shear banding resulting into an heterogeneous damage pattern along the shear band. At high confinement, pore pressure generation inside the band leads locally to fluidisation of the crushed material which results into the formation of connected channels in the heart of the band.

At large scale, similar phenomena are observed in faulted zones when sheared. Usually in fault zones, two main domains can be identified: a fault core of small thickness constituted of highly comminuted ultra-cataclasites is surrounded with a damage zone which consists of fractured host rock (e.g [51–53]). The ultracataclastic structure is the result of numerous earthquake ruptures. As shown for example in a recent study of Sulem et al. [54] dedicated to the characterisation of Aigion fault material in the Gulf of Corinth (Greece), the permeability of the fault core is very low so that this zone acts as an impervious barrier to transverse fluid flow, whereas the highly fractured damage zone around acts mostly as conduits for nearly along-strike flow. Similar observations can be found in the work of Wibberley and Shimamoto [53].

Acknowledgements

Appendix A. Shear band analysis of axisymmetric triaxial test

Extensive presentation of shear band analysis in geomaterials can be found in Vardoulakis and Sulem [34].

The constitutive equations of Mohr–Coulomb flow elastoplasticity theory are used here. In the coordinate system of principal axes of initial stress, the incremental equations are

$$\Delta\sigma_{11} = L_{11}\,\Delta\varepsilon_{11} + L_{12}\,\Delta\varepsilon_{22},$$
$$\Delta\sigma_{22} = L_{21}\,\Delta\varepsilon_{11} + L_{22}\,\Delta\varepsilon_{22},$$
$$\Delta\sigma_{12} = 2G\,\Delta\varepsilon_{12}, \tag{A.1}$$

where for axisymmetric compression:

$$L_{11} = G\left(\left(\kappa + \frac{4}{3}\right) - \frac{1}{H}\left(\frac{1}{\sqrt{3}} + \kappa f\right)\left(\frac{1}{\sqrt{3}} + \kappa d\right)\right),$$
$$L_{12} = G\left(\left(\kappa - \frac{2}{3}\right) - \frac{1}{H}\left(-\frac{2}{\sqrt{3}} + \kappa f\right)\left(\frac{1}{\sqrt{3}} + \kappa d\right)\right),$$
$$L_{21} = G\left(\left(\kappa - \frac{2}{3}\right) - \frac{1}{H}\left(\frac{1}{\sqrt{3}} + \kappa f\right)\left(-\frac{2}{\sqrt{3}} + \kappa d\right)\right),$$
$$L_{22} = G\left(\left(\kappa + \frac{4}{3}\right) - \frac{1}{H}\left(-\frac{2}{\sqrt{3}} + \kappa f\right)\left(-\frac{2}{\sqrt{3}} + \kappa d\right)\right). \tag{A.2}$$

In Eq. (A.1), G is the elastic shear modulus, $\kappa = 2(1+v)/3(1-2v)$ (v is the Poisson's ratio), $H = 1 + h + f\kappa d$ is the plastic modulus (h is the hardening modulus), f is the friction coefficient and d is the dilatancy coefficient. These parameters are deduced from the calibration of the elasto-plastic parameters on the triaxial test data.

The characteristic equation for the shear band inclination θ is

$$a\tan^4\theta + b\tan^2\theta + c = 0, \tag{A.3}$$

where θ is measured with respect to the minor principal axis direction and

$$a = L_{11},$$
$$b = (L_{11}L_{22} + G^2 - (L_{12} + G)(L_{21} - G)),$$
$$c = L_{22}. \tag{A.4}$$

The condition for shear band bifurcation is derived from the requirement that the above characteristic Eq. (A.3) has real solutions. This condition is firstly met at the state for which

$$b/a < 0 \text{ and } \Delta = b^2 - 4ac = 0. \tag{A.5}$$

Using the constitutive Eq. (A.2), Eq. (A.5) can be solved explicitly in terms of the critical hardening modulus h_B at shear banding,

$$h_B = \frac{1}{4}\kappa\frac{9\kappa(f^2 + d^2) - 2fd(15\kappa + 8) - 2\sqrt{3}(f + d + \sqrt{3}/2)(3\kappa + 4)}{9\kappa^2 + 15\kappa + 4}$$
$$\text{with } \frac{f + d + \sqrt{3}}{3\kappa(f + d) - \sqrt{3}(2 + 3\kappa)} < 0. \tag{A.6}$$

For axisymmetric compression, the friction coefficient f and the dilatancy coefficient d are expressed in terms of the mobilised friction angle ϕ and dilatancy angle ψ:

$$f = \frac{2\sqrt{3}\sin\phi}{3 - \sin\phi}, \quad d = \frac{2\sqrt{3}\sin\psi}{3 - \sin\psi}. \tag{A.7}$$

In a simplified analysis, we take here the values of the friction and dilatancy coefficients at peak stress. For the Fontainebleau sandstone Poisson's ratio is $v = 0.2$, the friction angle is $\phi = 41.3°$, and the dilatancy coefficient is fitted on the experimental data with a linear fit as a

function of the confining pressure σ_3 (Fig. 11):

$$d = d_1\sigma_3 + d_2 \qquad (A.8)$$

with $d_1 = -0.02$ and $d_2 = 1.32$

When the shear band bifurcation condition (A.5) is met two symmetric shear band directions exist given by

$$\theta_B = \pm \arctan(\sqrt[4]{(c/a)}). \qquad (A.9)$$

The critical hardening modulus h_B is plotted in Fig. 27 versus the confining pressure. In flow theory of elastoplasticity, it is obtained that for axisymmetric compression conditions, shear banding occurs in the
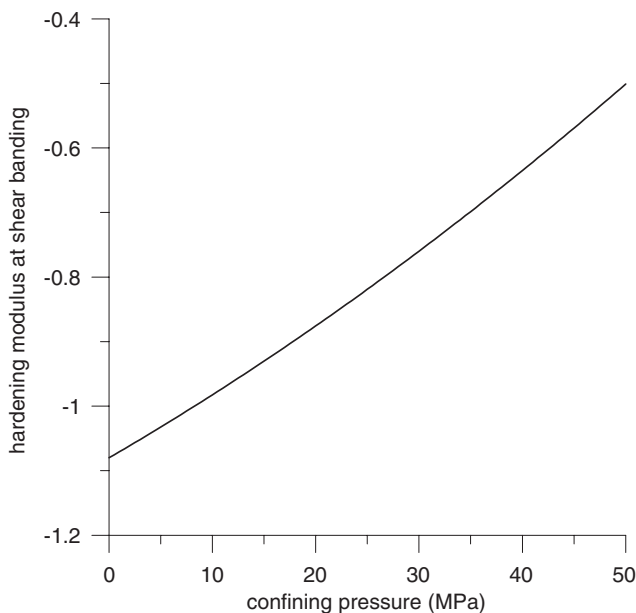
softening regime ($h < 0$) [34]. The corresponding shear band orientation is presented in Fig. 28.

Fig. 27. Critical hardening modulus at shear banding.
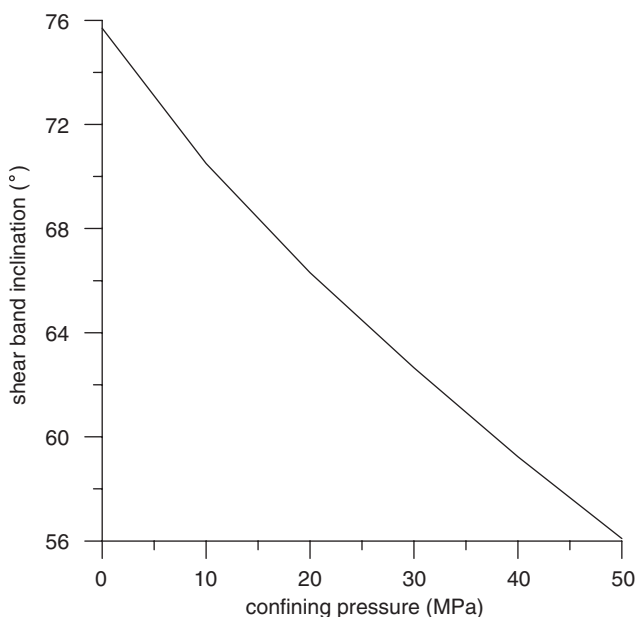
Fig. 28. Computed shear band orientation.

References

[1] Aydin A, Johnson AM. Analysis of faulting in porous sandstones. J Struct Geol 1983;5(1):19–31.

[2] Antonellini MA, Aydin A, Pollard D. Microstructure of deformation bands in porous sandstones at Arches National Park, Utah. J Struct Geol 1994;16(7):941–59.

[3] Menendez B, Zhu W, Wong T-f. Micromechanics of brittle faulting and cataclastic flow in Berea sandstone. J Struct Geol 1996;18(1):l–16.

[4] Wong T-f, David C, Zhu W. The transition from brittle faulting to cataclastic flow: mechanical deformation. J Geophys Res 1997;202:3009–25.

[5] Zhu W, Wong T-f. Permeability reduction in a dilatant rock: network modeling of damage and tortuosity. Geophys Res Lett 1996;23:3099–102.

[6] Zhu W, Wong T. The transition from brittle faulting to cataclastic flow: permeability evolution. J Geophys Res 1997;102:3027–41.

[7] Zhu W, Wong T. Network modeling of the evolution of permeability and dilatancy in compact rock. J Geophys Res 1999;104:2963–71.

[8] David C, Menendez B, Zhu W, Wong TF. Mechanical compaction, microstructures and permeability evolution in sandstones. Phys Chem Earth (A) 2001;26(1–2):45–51.

[9] Mair K, Main I, Elphick S. Sequential growth of deformation bands in the laboratory. J Struct Geol 2000;22:25–42.

[10] Main IG, Mair K, Kwon O, Elphick SC, Ngwenya BT. Experimental constraints on the mechanical and hydraulic properties of deformation bands in porous sandstones: a review. In: Holdsworth RE, Strachan RA, Magloughlin JF, Knipe RJ, editors. The nature and significance of fault zone weakening. Geol Soc Lond Spec Publ 2001; 186: 43–63.

[11] Bernabé Y, Mok U, Evans B. Permeability–porosity relationships in rocks subjected to various evolution process. Pure Appl Geophys 2003;160:937–60.

[12] Bésuelle P, Desrues J, Raynaud S. Experimental characterisation of the localisation phenomenon inside a Vosges sandstone in a triaxial cell. Int J Rock Mech Min Sci 2000;37(8):1223–37.

[13] Ord A, Vardoulakis I, Kajewski R. Shear band formation in Gosford sandstone. Int J Rock Mech Min Sci Geomech Abstr 1991;28(5):397–409.

[14] Ngwenya BT, Kwon O, Elphick SC, Main IG. Permeability evolution during progressive development of deformation bands in porous sandstones. J Geophys Res 2003;108(B7):2343–57.

[15] Fortin J, Schubnel A, Guégen Y. Elastic wave velocities and permeability evolution during compaction of Bleurswiller sandstone. Int J Rock Mech Min Sci 2005; in press. Available online 27 June 2005.

[16] Brace WF. Volumes changes during fracture and frictional sliding: a review. Pure Appl Geophys 1978;116:603–14.

[17] Zhang J, Wong T- F, Davis DM. Micromechanics of pressure-induced grain crushing in porous rocks. J Geophys Res 1990;95(B1):341–52.

[18] Cheng YP, Bolton MD, Nakata Y. Crushing and plastic deformation of soils simulated using DEM. Géotechnique 2004;54(2):131–41.

[19] Tsungui O, Vallet D, Charmet JC. Numerical model of crushing of grains inside two-dimensional granualar materials. Powder Technol 1999:190–8.

[20] Potyondy DO, Cundall PA. A bonded-particle model for rock. Int J Rock Mech Min Sci 2004;41:1329–64.

[21] Tang CA, Liu H, Lee PKK, Tsui Y, Tham LG. Numerical tests on micro–macro relation ship of rock failure under uniaxial compression—part I: effect of heterogeneity. Int J Rock Mech Min Sci 2000;37:555–69.

[22] Tang CA, Tham LG, Lee PKK, Tsui Y, Liu H. Numerical tests on micro–macro relation ship of rock failure under uniaxial compression—part II: constraint, slenderness and size effect. Int J Rock Mech Min Sci 2000;37:571–83.

[23] Yuan SC, Harrison JP. Modelling, enhanced fluid flow and fault sealing due to fracturing in heterogeneous rock. In: Barla G, Barla M, editors. Proceedings of the 11th IACMAG, vol. 2. 2005. p. 301–9.

[24] El Bied A, Sulem J, Martineau F. Microstructure of shear zones in Fontainebleau sandstone. Int J Rock Mech Min Sci 2002;39(7):917–32.

[25] Lock PA, Jing X, Zimmerman RW. Predicting the permeability of sandstone from image analysis of pore structure. J Appl Phys 2002;92(10):6311–9.

[26] Walsh JB, Brace WF. The effect of pressure on porosity and the transport properties of rock. J Geophy Res 1984;89(B11): 9425–31.

[27] Fairhurst CA, Hudson JA. Draft ISRM suggested method for the complete stress-strain curve for intact rock in uniaxial compression. Int J Rock Mech Min Sci Geomech Abstr 1999;36:279–89.

[28] Labuz JF. Bridell JMReducing frictional constraint in compression testing through lubrication. Int J Rock Mech Min Sci Geomech Abstr 1993;30:451–5.

[29] Papamichos E, Tronvoll J, Skjaestein A, Unander TE, Labuz JF, Vardoulakis I, Sulem J. Constitutive testing of a weak sandstone. Mech Cohes-Frict Mater 2000;5:1–40.

[30] El Bied A, Sulem J. Adaptation du mode opératoire pour la réalisation d'essais en compression « vraie » sur les roches. Rev Fr Géotechniq 2003;103:43–60.

[31] Zimmerman RW. Compressibility of sandstones. Amsterdam: Elsevier; 1991.

[32] Roger V, Desrues J, Viggiani G. Experiments on strain localisation in dense sand under isochoric conditions. In: Oka F, editor. Localisation and bifurcation theory for soils and rocks. Rotterdam: Balkema; 1998. p. 239–48.

[33] Tien YM, Lee DH, Juang CH. A study on the strain and pore water pressure characteristics of sandstone during repeated loading. In: Cundall et al., editors. Key questions in rock mechanics. Rotterdam: Balkema; 1988. p. 43–9.

[34] Vardoulakis I, Sulem J. Bifurcation analysis in geomechanics. Rotterdam, New York: Blackie Academic and Professional; 1995.

[35] Vardoulakis I. Deformation of water saturated sand: I. Uniform undrained deformation and shear banding. Géotechnique 1995;46:441–56.

[36] Vardoulakis I. Deformation of water saturated sand: II. The effect of pore-water flow and shear banding. Géotechnique 1995;46:0457–472.

[37] Santarelli FJ. Etude expérimentale de la bifurcation dans les roches. Rev Fr Géotechniq 1990;50:61–70.

[38] Tatsuoka F, Kim Y-S. Deformation of shear zone in sedimentary soft rock observed in triaxial compression. In: Chambon R, Desrues J, Vardoulakis I, editors. Localisation and bifurcation theory for soils and rocks. Rotterdam: Balkema; 1994. p. 181–8.

[39] Martin CD, Chandler NA. The progressive fracture of Lac du Bonnet granite. Int J Rock Mech Min Sci Geomech Abstr 1994;31:643–59.

[40] Diederichs MS, Kaiser P, Eberhardt E. Damage initiation and propagation in hard rock during tunnelling and the influence of near-face stress rotation. Int J Rock Mech Min Sci 2004;41:785–812.

[41] Hill R. Acceleration waves in solids. J Mech Phys Solids 1962;10:1–16.

[42] Arthur JRF, Dunstan T, Al-Ani QAJ, Assadi A. Plastic deformation and failure in granular media. Géotechnique 1977;42:395–410.

[43] Vardoulakis I. Shear band inclination and shear modulus of sand in biaxial tests. Int J Num Anal Meth Geomech 1980;4:3–119.

[44] Ioannidis MA, Kwiecien MJ, Chatzis I. Statistical analysis of the porous microstructure as a method for estimating reservoir permeability. J Petrol Sci Eng 1996;16:251–61.

[45] Liang Z, Ioannidas MA, Chatzis I. Permeability and electrical conductivity of porous media from 3D stochastic replicas of the microstructure. Chem Eng Sci 2000;55:5247–62.

[46] Cerepi A, Durand C, Brosse E. Pore microgeometry analysis in low-resistivity sabdstone reservoirs. J Petrol Sci Eng 2002;35:205–32.

[47] Fredrich JT, Greaves KH Mertin JW. Pore geometry and transport properties of Fontainebleau sandstone. Int J Rock Mech Min Sci Geomech Abstr 1993;30(7):691–7.

[48] Archie GE. The electrical resistivity log as aid in determining some reservoir characteristics. Trans Am Inst Mech Eng 1942;146:54–61.

[49] Bourbie T, Zinszner B. Hydraulic and acoustic properties as a function of porosity in Fontainebleau sandstone. J Geophys Res 1985;90(B13):11524–32.

[50] David C, Darot M. Permeability and conductivity of sandstones. In: Maury, Fourmaintraux, editors. Rock at great depth. Rotterdam: Balkema; 1989. p. 203–9.

[51] Chester FM, Chester JS. Ultracataclasite structure and friction processes of the Punchbowl fault, San Andreas system, California. Tectonophysics 1998;295:199–221.

[52] Micarelli L, Moretti I, Daniel JM. Structural properties of rift-related normal faults: the case study of the Gulf of Corinth, Greece. J Geodynam 2003;36:275–303.

[53] Wibberley C, Shimamoto T. Internal structure and permeability of major strike-slip fault zones: the Median Tectonic Line in Mie Prefecture, Southwest Japan. J Struct Geol 2003;25:59–78.

[54] Sulem J, Vardoulakis I, Ouffroukh H, Perdikatsis V. Thermo-poro-mechanical properties of the Aigion Fault clayey gouge—application to the analysis of shear heating and fluid pressurization. Soil Found 2005;45(2):97–108.